



NRL/FR/6111--97-9878

## Obscurants for Infrared Countermeasures

H.D. LADOUCEUR  
A.P. BARONAVSKI  
H.H. NELSON

*Chemical Dynamics and Diagnostics Branch  
Chemistry Division*

December 17, 1997

DTIC QUALITY INSPECTED 2

19980108 073

Approved for public release; distribution is unlimited.

REPORT DOCUMENTATION PAGE			Form Approved OMB No. 0704-0188	
Public reporting burden for this collection of information is estimated to average 1 hour per response, including the time for reviewing instructions, searching existing data sources, gathering and maintaining the data needed, and completing and reviewing the collection of information. Send comments regarding this burden estimate or any other aspect of this collection of information, including suggestions for reducing this burden, to Washington Headquarters Services, Directorate for Information Operations and Reports, 1215 Jefferson Davis Highway, Suite 1204, Arlington, VA 22202-4302, and to the Office of Management and Budget, Paperwork Reduction Project (0704-0188), Washington, DC 20503.				
1. AGENCY USE ONLY (Leave Blank)		2. REPORT DATE December 17, 1997		3. REPORT TYPE AND DATES COVERED
4. TITLE AND SUBTITLE Obscurants for Infrared Countermeasures			5. FUNDING NUMBERS PE-62270N	
6. AUTHOR(S) H.D. Ladouceur, A.P. Baranavski, and H.H. Nelson				
7. PERFORMING ORGANIZATION NAME(S) AND ADDRESS(ES) Naval Research Laboratory Washington, DC 20375-5320			8. PERFORMING ORGANIZATION REPORT NUMBER NRL/FR/6111--97-9878	
9. SPONSORING/MONITORING AGENCY NAME(S) AND ADDRESS(ES) Office of Naval Research 800 North Quincy Street Arlington, VA 22217-5660			10. SPONSORING/MONITORING AGENCY REPORT NUMBER	
11. SUPPLEMENTARY NOTES				
12a. DISTRIBUTION/AVAILABILITY STATEMENT Approved for public release; distribution is unlimited.			12b. DISTRIBUTION CODE	
13. ABSTRACT (Maximum 200 words)  The advent of imaging seekers in the 3-5 $\mu\text{m}$ and 8-12 $\mu\text{m}$ bands poses a new challenge in the area of infrared countermeasures. The next generation of seekers will be based on arrays that will provide the designer with a wide range of options for discriminating between enemy targets, friendly craft, and decoys. Area-extensive infrared countermeasures will be necessary to defeat these new seekers. One effective component of these countermeasures will be infrared absorbing particles, obscurants, essentially removing the original target from the imager's field. Our primary experimental concern in this study is to screen potential infrared obscurants as to their effectiveness, ease of deployment, chemical inertness, availability, cost, and environmental effects. Theoretical models that differentiate between scattering and absorption are also developed, and the results are compared to experimental measurements of extinction cross sections.				
14. SUBJECT TERMS Obscurants      Scattering Infrared        Particles			15. NUMBER OF PAGES 28	
			16. PRICE CODE	
17. SECURITY CLASSIFICATION OF REPORT UNCLASSIFIED	18. SECURITY CLASSIFICATION OF THIS PAGE UNCLASSIFIED	19. SECURITY CLASSIFICATION OF ABSTRACT UNCLASSIFIED	20. LIMITATION OF ABSTRACT UL	

## CONTENTS

EXECUTIVE SUMMARY .....	E-1
INTRODUCTION.....	1
TECHNICAL APPROACH.....	1
EXPERIMENTAL METHODS.....	2
EXPERIMENTAL RESULTS.....	4
THEORY .....	6
Particle Entrainment .....	6
Radiative Transfer Models.....	8
Brass Extinction Cross Section .....	14
Brass Absorbance Calculations .....	16
Boron Nitride Calculations.....	19
DISCUSSION .....	21
REFERENCES.....	22

## EXECUTIVE SUMMARY

The advent of imaging seekers in the 3-5  $\mu\text{m}$  and 8-12  $\mu\text{m}$  bands poses a new challenge in the area of infrared (IR) countermeasures. Area-extensive infrared countermeasures will be necessary to defeat these new seekers. Based on work by the Army, one effective component of these area-extensive IR countermeasures may be obscurants. These materials can degrade the scene image at the seeker. Our primary concern in this study is to identify potential IR obscurants and determine their extinction properties. Our initial concern is the 3-5  $\mu\text{m}$  atmospheric window; however, some of the materials also show promising characteristics in the 8-12  $\mu\text{m}$  window. We are also sensitive to potential environmental and health related issues, ease of procurement and use, and availability and cost. As a result, all initial candidates are readily available powders with acceptable toxicological and optical properties that are either known or can be readily determined from infrared absorption spectra.

We have designed and constructed an experimental apparatus to measure the extinction spectra of suspended particles. The apparatus consists of a venturi nozzle to lift the particles and mix them with nitrogen carrier gas. The gas/particle stream flows up a flow tube equipped with optical ports for Fourier Transform Infrared (FTIR) interrogation. Particle mass loading is calculated from the measured volume flow rate of the carrier gas and the mass consumption of the test powder. Using this apparatus, we have measured the mass extinction coefficients for brass flakes, 325 mesh boron nitride (BN) powder and 325 mesh boric acid. The mass extinction coefficients have been converted to volume extinction coefficients using published and measured packing densities of the individual materials.

In parallel with the experimental efforts, we have developed a series of codes to calculate the absorbance of suspended powders. The Mie theory provides detailed information about the scattering and absorption processes associated with individual particles in the obscurant cloud. The quantities calculated from Mie theory (cross sections, phase functions, etc.) can be related to experimental observations through the radiative transport equation. An analytic model has been developed to describe the IR absorbance in a cold slab geometry of suspended particles.

The mass extinction coefficient for brass powders has been determined from IR absorbance measurements and calculated by Mie theory using experimental optical constants. Our experimental and theoretical results for the mass extinction coefficient agree well, but are lower than that reported in the obscurant literature by a factor of 15.

We performed similar experimental and theoretical studies on BN powder, which was one of our initial candidates. We found that the spectra in the literature are incorrect. However, we have derived good optical constants to model its absorption and scattering. Although BN itself does not have strong resonances in the 3-5  $\mu\text{m}$  region, it does exhibit a strong resonance at 7.4  $\mu\text{m}$  ( $\sigma_{\text{ext}} = 0.27 \text{ m}^2/\text{gm}$ ) that tails into the 10  $\mu\text{m}$  region. This may, therefore, be useful in the long wave IR band. These results also confirm that our model can provide useful guidelines for predicting accurate cross sections for both scattering and absorption features through the entire IR, provided the complex index of

refraction and particle size distribution are available. We are confident that we can now use the theory to prefilter candidate materials, and provide specific guidelines concerning the optimum particle sizes.

To move the absorption into the 3-5  $\mu\text{m}$  region, boric acid was chosen for investigation. The presence of an OH chemical moiety results in a large absorption in this region, and boric acid can be obtained commercially as a fine powder (325 mesh). Although the spectra appear promising, the cross sections are too low (typically  $\sim 0.008 \text{ m}^2/\text{gm}$ ) for it to be an effective obscurant. However, it could be used for demonstration purposes or proof of principle tests. We are optimistic that this is not the best system available in this region, and are looking at several alternatives.

Extinction properties of each of the materials tested in both the 3-5  $\mu\text{m}$  and 8-12  $\mu\text{m}$  bands are shown in the table below. The fractional extinction shown in the table is calculated from the measured mass extinction coefficients vs wavelength, the mass loading calculated from the packing density and the assumed charge size ( $70 \text{ cm}^3$ ), and a path length of 10 m. The resulting wavelength-dependent extinction is multiplied by the blackbody curve for a 350K source in the 3-5  $\mu\text{m}$  and 8-12  $\mu\text{m}$  regions. The values tabulated are the average extinction in these two windows.

Fractional Extinction of Radiation from a 350K Blackbody Resulting from  $70 \text{ cm}^3$  of the Materials Investigated in This Study Dispersed in a 10-m Diameter Cloud

Material	Packing Density ( $\text{g}/\text{cm}^3$ )	Band	
		3-5 $\mu\text{m}$	8-12 $\mu\text{m}$
Brass flakes	2.6	0.22	0.22
Boron nitride	0.666	0.07	0.05
Boric acid	0.667	0.02	0.01

The methodology and approach we describe is both sound and practical and can be applied to a number of problems. We propose to extend this technique to other regions of the spectrum, including the near-IR, visible, and ultraviolet. These extensions are straightforward applications of the current experimental setup, with some additional optics to cover the expanded portions of the spectrum.

## OBSCURANTS FOR INFRARED COUNTERMEASURES

### INTRODUCTION

The advent of imaging seekers in the 3-5  $\mu\text{m}$  and 8-12  $\mu\text{m}$  bands poses a new challenge in the area of infrared countermeasures. Conventional seekers rely on the power received in a particular spectral region or regions, but they are not sensitive to the spatial extent, aspect ratio, or velocity of the perceived target. The next generations of seekers will be based on arrays that will provide the designer with a wide range of options for discriminating between enemy targets, friendly craft, and decoys. The simplest discriminants involve those relating to spatial extent and aspect ratio. Area-extensive infrared countermeasures will be necessary to defeat these new seekers. Based on work by the Army, one effective component of these area-extensive IR countermeasures could be obscurants. Our primary concern in this study is to screen potential infrared obscurants as to their extinction properties, ease of deployment, chemical inertness, availability, cost, and environmental effects.

An airborne obscurant modifies electromagnetic wave propagation between a potential target and a posed threat or observer. The radiation from the target can be removed from the threat's field of view by scattering and absorption processes. This reduction in radiance is classified as a direct transmission loss. The direct transmission loss depends on the obscurant's mass concentration, spatial distribution, particle size distribution, particle geometry, as well as its bulk optical properties, i.e., the complex index of refraction. The spectral signature of the obscurant cloud is affected by both the potential target and the environment. Forward scattering of radiation from the target contributes to the radiance of the obscurant cloud. Backward scattering, on the other hand, reduces the radiance. Diffuse multiple scattering within the obscurant cloud can introduce radiation from point sources such as the sun or extended sources such as the sky or natural cloud cover. These background sources contribute to the obscurant cloud's radiance. Our objective in this program is to find materials that will, with some combination of scattering and absorption, remove spectral radiance in specific infrared windows. Initially, our concern is the 3-5  $\mu\text{m}$  window; however, some of the initial candidates also show promise in the 8-12  $\mu\text{m}$  window. We are also sensitive to potential environmental and health related issues, ease of procurement and use, and availability and cost. As a result, all our initial candidates will be readily available powders with acceptable toxicological properties and optical properties which are either known or can be readily determined from infrared absorption spectra.

### TECHNICAL APPROACH

This project encompasses a strong interaction of experimental and theoretical work. The major thrust of the FY97 effort was the identification of potential materials for deployment in a transmission loss infrared obscurant mode. The materials evaluated included both metals and refractory substances. The metal chosen for study was brass in the form of flakes, as used by the Army in their obscurant program. This species was chosen to provide a baseline for both the experimental and theoretical studies to follow. As discussed below, at this point we do not consider brass a viable candidate for several

reasons. However, it did provide us with the opportunity to confirm our experimental and theoretical methodology. The other materials studied included boron nitride (BN) and boric acid (BA). The boron nitride was originally chosen because of an apparent absorption peak in the 4  $\mu\text{m}$  region. This peak was reported by Doll (1994), but our work has conclusively shown that it is, in fact, not due to BN. This issue will be addressed in the discussion. Chemically, BN is a refractory material that is relatively inert. It reacts very slowly in humid air to produce boron oxides and ammonia. Spectra of boric acid taken by us exhibit relatively strong absorptions in both the 3-5  $\mu\text{m}$  and 8-12  $\mu\text{m}$  regions. Boric acid is an extremely weak acid ( $\text{pH} = 5.2$  for a 0.1N solution), which is not much different from the acidity found in pure water saturated with carbon dioxide (seltzer water). It is listed as an irritant, as most powders are, but chemically is relatively stable. Neither BN nor BA are considered environmentally hazardous.

The preliminary theoretical effort was directed at evaluating spectral scattering and absorption cross sections of proposed obscurants. The cross sections as a function of IR wavelength and particle size were calculated from experimental values of the complex index of refraction using the Mie theory for scattering from spheres. These calculations provided information on the relative importance of scattering and absorption processes for a proposed material. The ratio of the scattering cross section to the sum of the scattering and absorption (extinction) cross section is the single-scattering albedo. If the albedo is small ( $\ll 1$ ), the spectral transmittance of the obscurant cloud can be readily calculated from the particle concentration and the extinction coefficient using the exponential Lambert-Beer law.

The experimental effort measured the extinction coefficients of proposed obscurants. A gas flow reactor has been built that creates a suspension of particles of known size distribution and composition. The extinction of IR radiation from a black-body source by the suspended particles is measured using an Fourier Transform Infrared (FTIR) spectrometer. Contributions to the extinction from both scattering and absorption are measured, and the theoretical model is used to determine the albedo and particle size distributions. It is anticipated that the particle size distributions can ultimately be tailored to obtain the best combination of scattering vs absorption in the spectral regions of interest. In this way, some spectral tailoring of the obscurant can be accomplished. In all cases, spectral measurements are compared with the theoretical calculations discussed above. With guidance from these calculations, we plan to iterate on the particle size distributions and chemical nature of the obscurant to find the optimum material.

## EXPERIMENTAL METHODS

The experiments were carried out in an aerosol flow tube coupled to an FTIR spectrometer (Fig. 1). Briefly, powders for study flow up an aerosol flow tube where they intersect the beam of the FTIR spectrometer (Mattson Instruments, Cygnus 100) operating with an external detector. Transmission spectra are recorded with and without particle flow, and the resulting absorption due to the particles is plotted vs wavelength in the 2-20  $\mu\text{m}$  region.

Powders to be tested are picked up using a venturi nozzle (Air-Vac Engineering Company, Inc., model TD110H) operating with compressed nitrogen as the feed gas. The nozzle is designed such that 20 standard liters per minute (SLPM) of feed gas produces a vacuum flow of  $\sim 20$  SLPM. Powder is delivered to the vacuum inlet of the nozzle by a rotating platen feeder system. It consists of a 15-cm diameter rotating Al platen with a 1 cm wide  $\times$  1.2 cm deep groove at a radius of 6 cm. Powder is fed into this groove opposite the venturi feed tube, and the powder level is adjusted using a micrometer-controlled scraper. The platen rotates at 0.08 revolutions per second. As the platen rotates and the powder approaches the venturi nozzle, it is lifted by the vacuum flow through a 6 mm tube into the nozzle where it is mixed with the feed gas. Most experiments are conducted with a total flow (feed gas plus vacuum flow)

of 40 SLPM. Mass loading is calculated by dividing the measured mass consumption rate by this flow rate. Several experiments were also carried out at flows of 20 and 80 SLPM. At the highest flow, window contamination became a problem and these data were not used in the analysis.

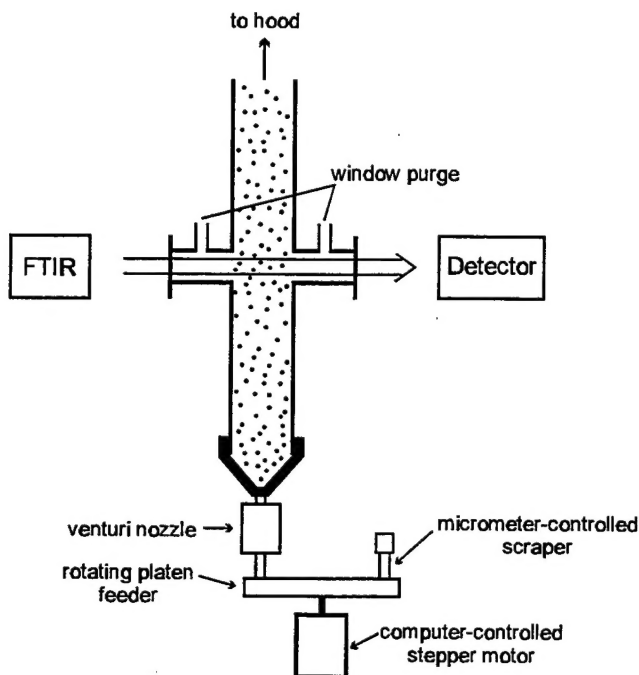


Fig. 1 – Schematic diagram of the apparatus used in this work

After exiting the venturi nozzle, the combined gas and particle flow enters a transition funnel that increases the area of the flow stream and lowers the linear flow velocity. As shown in Fig. 1, this funnel contains the main flow tube, which is a 11.4-cm inside diameter (ID) plexiglass tube. Two sidearms for the optical windows are located on opposite sides of the flow tube, 35 cm upstream of the transition funnel. The windows are set back 13 cm from the wall of the main flow tube. A nitrogen purge flow of 1.2 SLPM is split between the two sidearms to ensure that the powder does not deposit on the optical windows. After passing through the probe region, the particle flow is exhausted into the fume hood.

The IR probe beam is directed out of the spectrometer using a spherical mirror with 2-m radius of curvature. This results in a nearly collimated beam that propagates through the chamber and is focused on an HgCdTe detector. The spectra are recorded in single-beam mode from 400 to 5000  $\text{cm}^{-1}$  (25 to 2  $\mu\text{m}$ ), with a spectral resolution of 1  $\text{cm}^{-1}$ . Each spectrum recorded is the summation of 24 individual scans. Particulate extinction spectra are calculated by normalizing the single beam spectrum measured during powder flow by a background spectrum collected with only gas flowing. These spectra reflect not only particle absorption but any loss due to scattering, so they are true measures of the extinction coefficient of the particles.



## EXPERIMENTAL RESULTS

Absorption spectra of three candidate species have been measured over the 2-14  $\mu\text{m}$  spectral region under several different flow rates and particle loadings. Figure 2 is a representative spectrum of brass. All experimental data are presented in absorbance units (absorbance  $\equiv -\log(I/I_0)$ ). Our goal in measuring the brass extinction was to have a system to use as a benchmark for future studies. It has a relatively unstructured extinction coefficient throughout the IR, possibly indicating the dominance of scattering over any spectral absorption features. As such, it is not as attractive an obscurant as some of the other species to be discussed. It has, however, been used by the Army. When this program started, it was thought to be a well characterized particulate system (Edwards et al. 1992). However, the data shown are not consistent with the reported mass extinction coefficients, but are about a factor of 15-20 lower. Different flow rates and particle loadings had virtually no effect on the mass extinction coefficients determined from our experimental data. The large discrepancy between our numbers and those reported by Edwards et al. led us to explore some of the potential problems areas inherent in these measurements, i.e., multiple scattering, particle resonances, and scattering anisotropy. The theoretical model and results are discussed in the following section, however, the results from theoretical calculations support our measured extinction coefficients. At this time, we are not able to explain the Army's data with any certainty. It does appear from the available literature that the combination of path length and mass loading in the Army's experiment results in an absorption of  $>98\%$  of the IR radiation incident on their detector. In this case, it is quite possible that the measurements are in error due to the noise floor of the detector/amplifier or some saturation effect. Without additional details on the exact experimental configuration, it is impossible to elaborate further.

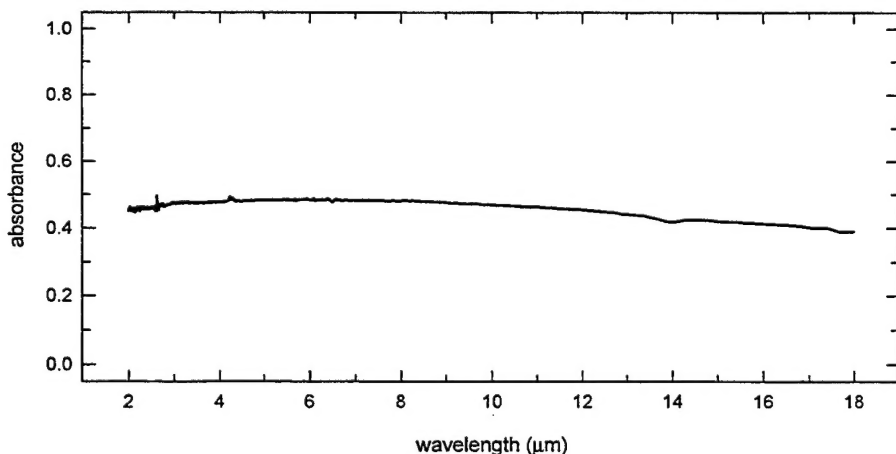


Fig. 2 – Experimental absorption spectrum of brass flakes at  $135 \text{ g/m}^3$  and a pathlength of 11.4 cm

The prime candidate at the beginning of this program was BN. It has several advantages over brass. It is readily available as a well-characterized powder, with a mass weighted distribution peaking at 10  $\mu\text{m}$  diameter particle size. It is non toxic, poses no environmental hazard, and is chemically stable. According to Doll (1994), there is a strong absorption feature in the 3-4  $\mu\text{m}$  region. Figure 3 shows an absorption spectrum of BN; no absorption band is evident in this spectral region. The large rising absorption in the 2  $\mu\text{m}$  region is thought to be due solely to scattering.

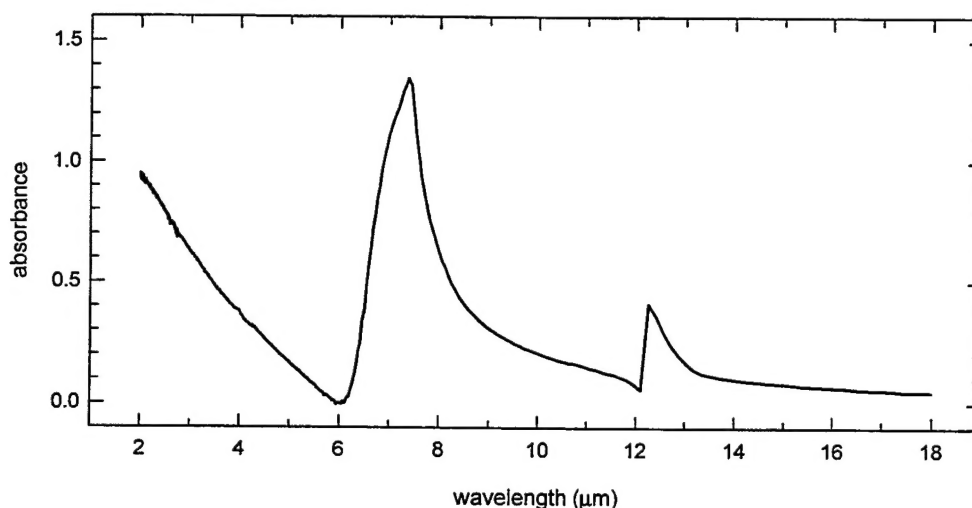


Fig. 3 – Experimental absorption spectrum of 325 mesh BN powder at  $98 \text{ g/m}^3$  using a 11.4 cm path length

There are other interesting features, however. The strong absorption feature at  $7.38 \text{ }\mu\text{m}$  carries well into the  $8\text{--}12 \text{ }\mu\text{m}$  region and is potentially useful against seekers in this region. To test the apparatus for linearity, a series of experiments at various flow rates and BN particle loadings was undertaken. These results are shown in Fig. 4 for data taken in three spectral regions. It is evident from the figure that, at the flow rates being used, the data are linear over at least an order-of-magnitude change in particle loading. Thus we can be confident that these data can be extended to the much lower concentrations and much longer path lengths that will be encountered in actual deployment tests.

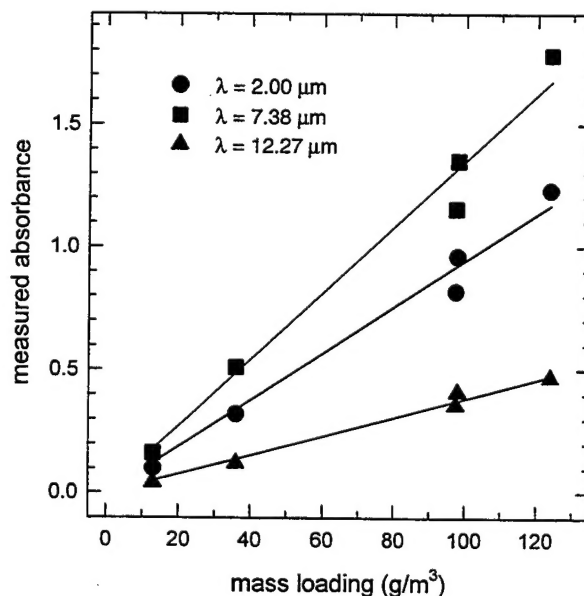


Fig. 4 – Measured absorbance of BN powder at three wavelengths vs mass loading. The points at  $98 \text{ g/m}^3$  correspond to volume flow rates of 20 and 40 SLPM.

To move the absorption into the 3-5  $\mu\text{m}$  region, boric acid was chosen. The presence of an OH chemical moiety results in a large absorption in this region, and boric acid can be obtained commercially as a fine powder (325 mesh). Figure 5 shows a spectrum of BA particulates. It is obvious that strong absorption features are present in the 3-6  $\mu\text{m}$  and 7-11  $\mu\text{m}$  regions. At the present time, we do not have an accurate particle size determination for the BA samples or optical constants for this material, but these can be determined and optimized. However, more work must be done to determine the best particle size distribution for a particular spectral region. These preliminary data are very encouraging and warrant additional study of BA as an obscurant.

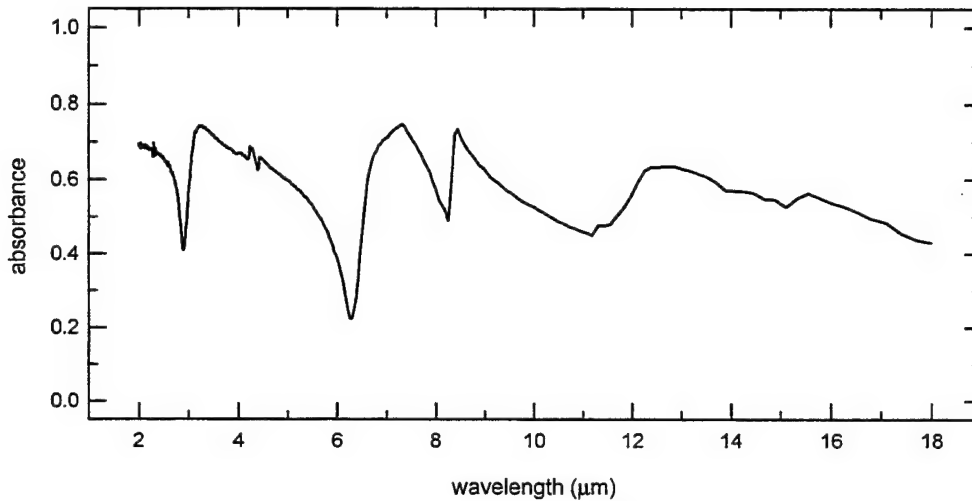


Fig. 5 – Experimental absorption spectrum of boric acid powder at  $750 \text{ g/m}^3$  and 11.4 cm pathlength

## THEORY

### Particle Entrainment

The nature of the gas-particle flow in the aerosol flow tube described above depends on the particle size distribution, the particle geometry and density, the gas viscosity, the inlet velocity, and the chamber geometry. Particles of different sizes or weight can be sorted by the flowing gas. Viscous effects of the gas are important near the tube walls and at the particle surfaces. A cylindrically symmetric stream function model (Zucrow and Hoffman 1976) has been developed to describe the gas flow within the chamber. The stream function ( $\Psi$ ) satisfies the continuity equation for the conservation of total mass in cylindrical coordinates:

$$\frac{\partial}{\partial z}(\rho r V_z) + \frac{\partial}{\partial r}(\rho r V_r) = 0$$

$$\frac{\partial \Psi}{\partial z} = -r \rho V_r \quad \frac{\partial \Psi}{\partial r} = r \rho V_z$$

$$\nabla^2 \Psi = 0,$$

where  $\rho$  is the gas density and  $V_r$  and  $V_z$  denote the radial and axial velocity, respectively. The radial component of velocity is nonzero in the conical base region of the test chamber. For subsonic (Mach number  $\ll 1$ ) or incompressible flow, the stream function is a solution of Laplace's equation subject to inlet and outlet boundary conditions. The velocity components are calculated from the spatial derivatives of  $\Psi$ . Since the tube diameter is large (11.4 cm), the stream function model should provide a reasonable approximation to the flow field throughout most of the tube volume. However, gas viscosity is neglected in this model, and therefore it fails to predict the zero-velocity (no-slip) condition near the tube walls. Corrections for the effects of gas viscosity on the flow could be included by using a boundary-layer model near the chamber surfaces. The deposition of particles on the chamber walls is due to the loss of "lift" that occurs within the boundary layer. Since we are primarily interested in the bulk flow away from surfaces, the boundary-layer model is not required. The key results of the stream function model calculations are given in Table 1 as functions of the inlet flow rate. These results were obtained from numerical solutions of the Laplace equation using a finite-element code (PDEase 1995).

Table 1 – Results of the Stream Function Model Calculations

Flow rate (liter/min)	Inlet Speed (cm/s)	$V_z$ (cm/s)	Mass Flow Rate (gm/s)
20	1052	2.63	0.374
40	2105	5.26	0.749
80	4210	10.52	1.497

Over the range of inlet flow rates considered, the axial velocity ( $V_z$ ) drops by a factor of 400 within 2.0 cm of the inlet exit. Upon leaving the conical base region, the model predicts a uniform plug flow up the tube. This plug flow provides "lift" for the particles. The force acting upward on a single particle of diameter  $d$  is given by (Zhou 1993)

$$F_{up} = C_d \pi \frac{d^2}{4} \rho \frac{|\bar{v}_g - \bar{v}_p|}{2} (V_g - V_p),$$

where  $C_d$  is the drag coefficient,  $V_g$  denotes the gas stream speed, and  $V_p$  is the particle speed. In the Stokes regime, the drag coefficient for a spherical particle is given by

$$C_d = \frac{24\nu}{|\bar{v}_g - \bar{v}_p|d} = \frac{24}{\text{Re}},$$

where  $\nu$  is the kinematic viscosity ( $\text{N}_2/0.1586 \text{ cm}^2/\text{s}$  @ 300K) of the gas and  $\text{Re}$  is the Reynolds number. This expression for the drag coefficient is valid for Reynolds numbers below 0.2 (creeping flow). The Reynolds numbers for the particles considered here are on the order of  $1 \times 10^{-4}$ . The drag coefficient for a disk is very similar to that of the sphere (*Chemical Engineers' Handbook* 1973). Thus, the analysis is applicable to brass flakes modeled as falling circular disks.

The gravitational force (weight) acting downward on an individual spherical particle is given by

$$F_{dn} = \rho_p g \frac{\pi d^3}{6},$$

where  $\rho_p$  is the bulk particle density ( $8.5 \text{ gm/cm}^3$  for brass) and  $g$  is the gravitational constant. The magnitudes of these forces are plotted in Fig. 6 as a function of brass particle diameter for various flow rates. The lifting force is a linear function of particle diameter. The weight increases as the cube of the diameter. The forces are balanced where the lines intersect the weight curve. Particles whose diameters lie to the left of the intersections are accelerated upward in the gas stream. Particles whose diameters are to the right of the intersections fall downward. The absolute velocity of a particular particle depends on its terminal velocity as well as the gas speed. If the downward terminal velocity is equal to the upward gas speed, the particle is suspended, having an absolute velocity of zero. These calculations assume an equilibrium flow in which the particle's diffusion relaxation time is very short compared with the residence time in the chamber. The chamber residence time is on the order of 17 s at 40 SLPM and the diffusional relaxation times are on the order of  $10^{-4}$  to  $10^{-6}$  s. This relaxation time implies that the particles respond quickly to the flow field and are able to track the streamlines.

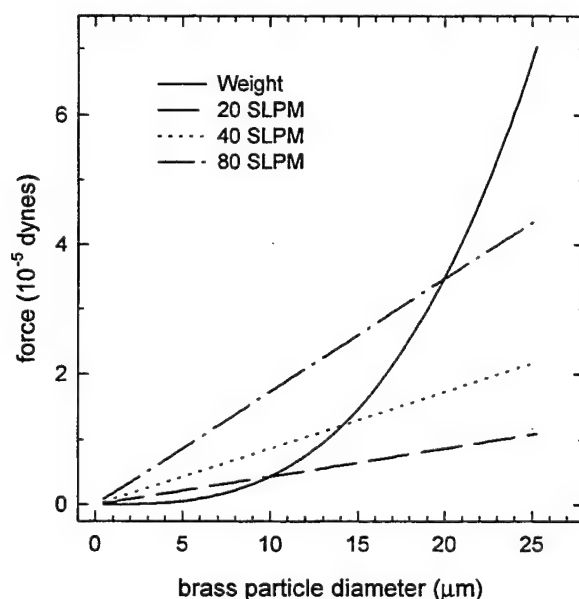


Fig. 6 – The calculated weight of spherical brass particles and the lift force they experience at three flow rates appropriate to this study

The calculations reveal that at 40 SLPM the largest spherical brass particle we can “pick up” is about 14  $\mu\text{m}$  in diameter. If the brass flakes are modeled as circular disks of 1.7  $\mu\text{m}$  diameter with a thickness of 0.08 to 0.32  $\mu\text{m}$ , the weight is on the order of  $1.0 \times 10^{-9}$  dynes. This weight is four orders of magnitude smaller than the estimated lift forces and therefore, all flakes should be entrained in the main gas stream.

### Radiative Transfer Models

An airborne obscurant material modifies electromagnetic wave propagation between a potential target and a posed threat or observer. The radiation from the target can be removed from the threat's field of view by scattering and absorption processes. Each of these processes has a spectral cross section ( $\text{cm}^2$ )

associated with it, which is a function of particle geometry, wavelength, and the particle's complex index of refraction. The sum of the spectral absorption cross section ( $\sigma_{ab}$ ) and the spectral scattering cross section ( $\sigma_{sc}$ ) is the spectral *extinction cross section* ( $\sigma_{ex}$ ). The albedo, denoted by  $\omega$ , is the ratio of the scattering cross section to the extinction cross section

$$\omega \equiv \frac{\sigma_{sc}}{\sigma_{sc} + \sigma_{ab}}$$

The numerical value of the single-particle albedo indicates the importance of scattering. An albedo of one implies that the obscurant acts purely as a scattering medium in which no absorption or emission occurs at the given wavelength. An albedo of zero indicates a purely absorbing and/or emitting medium with no scattering. Both the albedo and cross sections depend implicitly on the radiation wavelength  $\lambda$  and polarization. In general, both absorption and scattering processes occur simultaneously within the cloud, and the albedo lies somewhere between zero and one. The loss in radiant intensity ( $I$ ) along a line of sight (LOS) through the obscurant cloud is classified as a *direct transmission loss* and is governed by the radiative transfer equation. The direct transmission loss depends on the obscurant's mass concentration, spatial distribution, particle size distribution, particle geometry, and the bulk optical properties, i.e., the particle's complex index of refraction.

The spectral signature of the obscurant cloud is affected by both the potential target and the environment. Forward scattering of radiation from the target contributes to the obscurant cloud's radiance (intensity). Diffuse multiple scattering within the cloud can introduce radiation from point sources such as the sun or extended sources such as the sky or natural cloud cover. These background sources all contribute to the obscurant cloud's radiance.

The Mie theory provides detailed information about the scattering and absorption processes associated with individual particles in the obscurant cloud. The quantities calculated from Mie theory (cross sections, phase functions, etc.) can be related to experimental observations through the radiative transport equation. An analytic model is now developed to describe the IR absorbance in a cold slab geometry of suspended particles (Fig. 7).

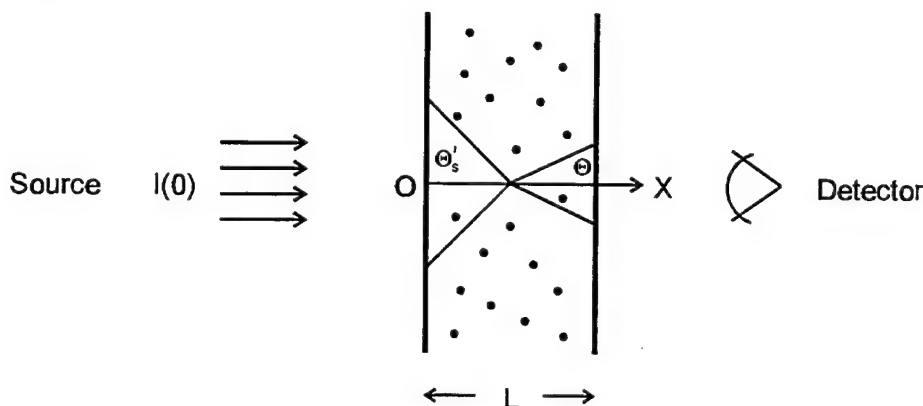


Fig. 7 - Schematic illustrating the slab geometry used in the absorbance calculations

The radiative transfer equation for an isotropic slab of thickness  $L$  with azimuthal symmetry is given by (Ozisik 1972)

$$\mu \frac{dI}{dx} = -N_p(\sigma_{ab} + \sigma_{sc}) \cdot \left( I(x, \mu) - \frac{\omega}{2} \int_{-1}^1 p(\mu, \mu') \cdot I(x, \mu') d\mu' \right),$$

where  $\mu$  is the cosine of the angle  $\theta$  between the direction of the radiation intensity and the positive OX axis through the slab,  $N_p$  is the number of particles per unit volume ( $1/\text{cm}^3$ ),  $\mu'$  denotes the cosine of the in-scattering angle  $\theta'_s$ , and  $p(\mu, \mu')$  is the *phase function*. The phase function, which depends on wavelength  $\lambda$ , the particle diameter, and the material's optical constants, provides information about the directional distribution of scattered radiation. For the slab geometry considered here, the phase function describes scattering from the  $\mu'$  direction (a cone of incident directions making an angle of  $\theta'_s$  with the OX axis) into the  $\mu$  direction (a cone of scattering directions making an angle of  $\theta$  with the OX axis). In the laboratory, the absorbance measurements are done at  $\theta = 0$  ( $\mu = 1$ ), but the in-scattering angle varies from 0 to 180 deg. If the particle size distribution is known within the cloud, the extinction coefficient ( $\gamma = N_p[\sigma_{ab} + \sigma_{sc}]$ ) and phase function are calculated by a suitable average over the given particle distribution.

The first term on the right-hand side of the radiative transfer equation represents the *loss* in radiant intensity  $I$  due to absorption and scattering out of the line of sight (LOS). The last integral term represents the *gain* in radiant energy by the beam along the LOS due to in-scattering of radiation by the surrounding obscurant. The in-scattering term decreases the obscurant cloud's absorbance. The efficiency of in-scattering to increase the radiant intensity depends on the phase function and the magnitude of the albedo  $\omega$ . The phase function is often represented by expansions in Legendre polynomials ( $P_n(x)$ ) of the form

$$p(\mu, \mu') = \sum_{n=0}^N a_n P_n(\mu) P_n(\mu')$$

where  $a_0 = 1$ . The relation between the slab variables ( $\mu', \mu$ ) and the single-particle phase function calculated from Mie theory can be obtained from solid geometry.

If the obscurant particles are assumed to be spherical, homogeneous, and isotropic, the Mie scattering theory can be used to calculate the spectral absorption and scattering cross sections, the albedo, and the phase functions for the specified particle size. In general, the obscurant particles are not all the same size (monodispersed), and the Mie calculations would have to be done with a given particle distribution function. Since we have no information on the particle size distribution for the brass flakes,  $N_p$  denotes the number of monodispersed particles per cubic centimeter.

When the albedo is less than one, the radiative transfer equation can be solved for the spectral intensity by a perturbation series in  $\omega$

$$I(x, \lambda) = I_0 + \omega \cdot I_1 + \omega^2 \cdot I_2 + \dots$$

Substitution of this series solution into the radiative transfer equation yields in lowest order the Lambert-Beer law

$$\frac{dI_0}{dx} = -\frac{N_P(\sigma_{ab} + \sigma_{sc}) \cdot I_0}{\mu} \equiv -\frac{\gamma \cdot I_0}{\mu}$$

$$I_0(x, \mu) = I(0) \cdot \exp\left[\frac{-\gamma \cdot x}{\mu}\right]$$

$$A(\lambda, x, \mu) = -\log_{10}\left(\frac{I_0(x, \mu)}{I(0)}\right)$$

where  $I(0)$  denotes the initial spectral intensity and  $A(\lambda, x, \mu)$  is the Lambert-Beer spectral absorbance. The product  $N_P(\sigma_{ab} + \sigma_{sc}) = \gamma$  defines the spectral extinction coefficient in units of  $\text{cm}^{-1}$ .

When the phase function is represented by a simple analytic expression, e.g., the Legendre expansion, the solution  $I_0$  can be substituted into the in-scattering integral and the first-order correction  $I_1$  obtained in closed form. The simplest phase function is for *isotropic* scattering ( $p = 1$ ) for which the spatial distribution of scattered radiation about the scattering center (particle) is uniform. The phase function for *Rayleigh scattering* of unpolarized radiation is  $p(\theta_p) = 3/4(1 + \cos^2 \theta_p)$ , where  $\theta_p$  denotes the particle's single-scattering polar angle.  $\theta_p$  is the angle between the in-scattering direction and the out-scattering direction in the particle's frame of reference. The Rayleigh scattering distribution has equal "lobes" in the forward and backward direction about the scattering center. Figure 8 presents calculated phase functions for brass spheres of different diameters at  $\lambda = 4.0 \mu\text{m}$  and  $10.0 \mu\text{m}$ . At  $\lambda = 4.0 \mu\text{m}$ , the Mie scattering is very *anisotropic* for larger particles. Forward scattering ( $0 < \theta_{sc} < 90$ ) is favored over backward scattering for the  $4.83 \mu\text{m}$  and  $2.90 \mu\text{m}$  diameter particles. The phase function's angular dependence is weak for particle diameters  $< 1.5 \mu\text{m}$ . In the  $3\text{--}5 \mu\text{m}$  band, the small particle phase functions are almost isotropic. At  $\lambda = 10.0 \mu\text{m}$ , the phase functions for the smaller particles are very similar, while the larger particle diameters now display stronger backscattering. If the extinction is dominated by scattering, the measured absorbance depends strongly on the magnitude of the in-scattering integral.

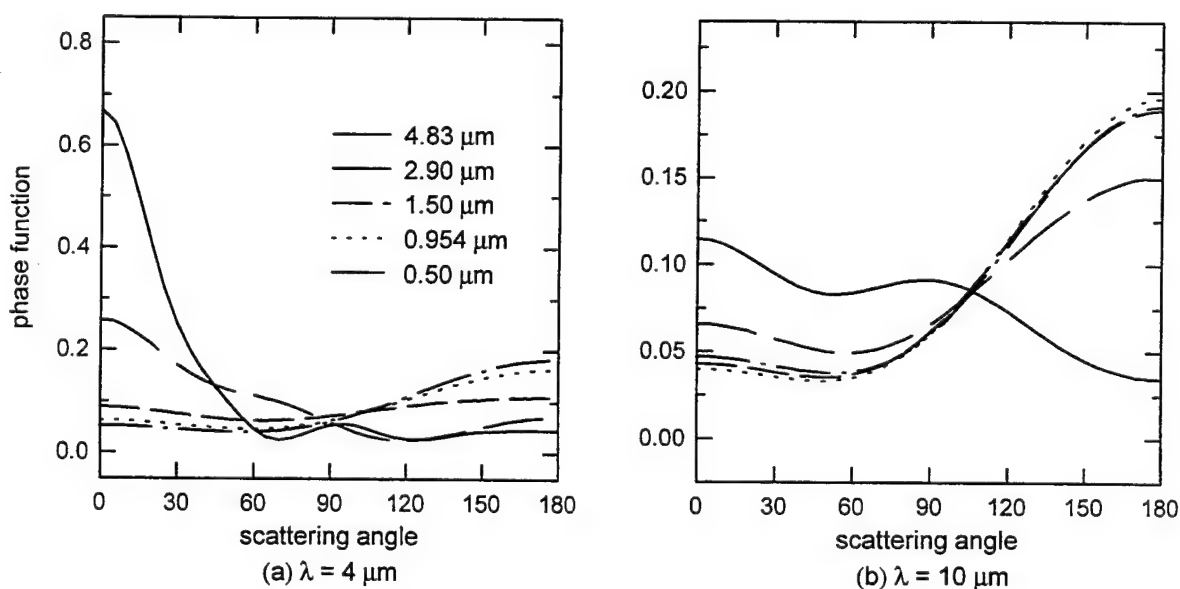


Fig. 8 – Calculated phase functions of brass spheres of different diameters



Higher-order corrections to the Lambert-Beer Law can be obtained from perturbation theory, but they are cumbersome and usually require numerical evaluation of the in-scattering integrals. Rather than deal with the full phase function over all wavelengths, it is sometimes more convenient and useful to consider some moment of the angular distribution that describes the relative forward-to-backward scattering ratio. The *asymmetry factor*  $g$  is defined as

$$g = \frac{1}{4\pi} \int_{4\pi} p \cdot \cos \theta \, d(\cos \theta).$$

The value of  $g$  ranges from  $-1$  (maximum backward scattering) to  $+1$  (maximum forward scattering). The calculation of this quantity as a function of wavelength provides insight into the spectral variation of the phase function. Figure 9 gives calculated asymmetry parameters for brass spheres of various diameters as a function of wavelength. The larger diameter particles tend to scatter the 3-5  $\mu\text{m}$  radiation in the forward direction ( $g > 0$ ) and the 8-12  $\mu\text{m}$  radiation in the backward direction ( $g < 0$ ) for diameters  $< 2.9 \mu\text{m}$ . The smaller diameter particles act as backscatters over the entire spectral region.

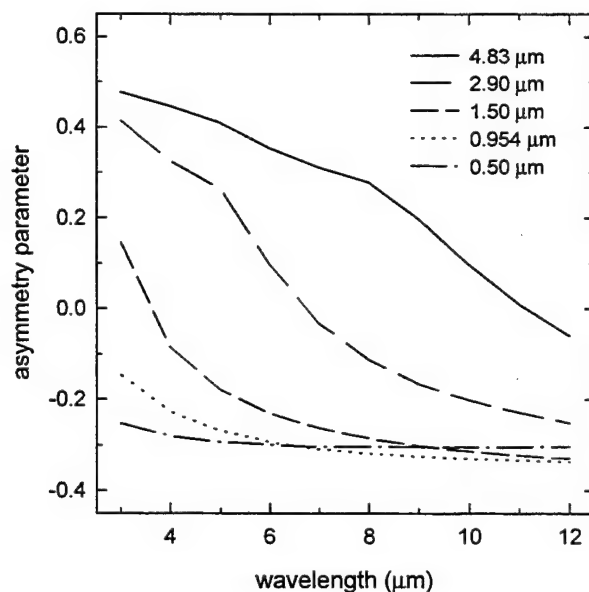


Fig. 9 – Calculated asymmetry parameters for brass spheres of various diameters as a function of wavelength

Scattering effects should be incorporated into the radiative transfer model for accurate calculation of absorbance and interpretation of experimental measurements. The presence of the in-scattering integral term in the radiative transfer equation presents the primary difficulty in solving the equation for radiant intensity. The way in which this term is treated distinguishes the various methods of solution (Brewster 1992). One of the simplest techniques is the two-flux method. The two-flux method groups all scattering into either the plus or minus  $x$  direction along a LOS. Assuming axial symmetry, the equation of radiative transfer along the LOS is replaced by two linear equations

$$\begin{aligned}\frac{dI^+}{dx} &= -\gamma \left( I^+ - \frac{\omega}{2} \int_0^\pi f(\theta) \cdot I'(x, \theta) \cdot \sin \theta d\theta \right) \\ \frac{dI^-}{dx} &= \gamma \left( I^- - \frac{\omega}{2} \int_0^\pi f(\theta) \cdot I'(x, \theta) \cdot \sin \theta d\theta \right) \\ \gamma &\equiv N_p (\sigma_{ab} + \sigma_{sc})\end{aligned}$$

where  $I^+$  and  $I^-$  denote the spectral radiation intensity at the distance  $x$  along the LOS in the directions of increasing and decreasing  $x$ , respectively,  $I'(x, \theta)$  is the radiation intensity reaching a scattering center at the angle  $\theta$  with respect to the LOS, and  $f(\theta)$  is the scattering angular distribution at the angle  $\theta$ . In the single-scattering approximation,  $f(\theta)$  is the phase function obtained from Mie theory. The integral in the above equations is now replaced by

$$\begin{aligned}\int_0^\pi f(\theta) \cdot I'(x, \theta) \cdot \sin \theta d\theta &= I_s^+(x) \cdot \int_0^{\pi/2} f(\theta) \cdot \sin \theta d\theta + I_s^-(x) \cdot \int_{\pi/2}^\pi f(\theta) \cdot \sin \theta d\theta \\ I_s^+(x) &\equiv \frac{\int_0^{\pi/2} f(\theta) \cdot I'(x, \theta) \cdot \sin \theta d\theta}{\int_0^{\pi/2} f(\theta) \cdot \sin \theta d\theta} \quad I_s^-(x) \equiv \frac{\int_{\pi/2}^\pi f(\theta) \cdot I'(x, \theta) \cdot \sin \theta d\theta}{\int_{\pi/2}^\pi f(\theta) \cdot \sin \theta d\theta}\end{aligned}$$

where  $I_s^+(x)$  and  $I_s^-(x)$  correspond to the forward and backward scattering intensity, respectively. The two-flux model assumes that  $I_s^+(x) = I^+(x)$  and  $I_s^-(x) = I^-(x)$ . This assumption reduces the system of integro-differential equations to coupled ordinary differential equations

$$\begin{aligned}\frac{dI^+}{dx} &= -N_p(\sigma_{ab} + \sigma_{sc}) \cdot I^+ + N_p\sigma_{sc}\alpha \cdot I^+ + N_p\sigma_{sc}\beta \cdot I^- & I^+(0) &= I(0) \\ \frac{dI^-}{dx} &= N_p(\sigma_{ab} + \sigma_{sc}) \cdot I^- - N_p\sigma_{sc}\alpha \cdot I^- - N_p\sigma_{sc}\beta \cdot I^+ & I^-(L) &= 0\end{aligned}$$

where  $\alpha \equiv 2\pi \int_0^{\pi/2} f(\theta) \cdot \sin \theta d\theta$  and  $\beta \equiv 2\pi \int_{\pi/2}^\pi f(\theta) \cdot \sin \theta d\theta$ . Note that the  $\alpha$  and  $\beta$  terms have opposite

signs from the loss terms in each equation and increase the radiation intensity along the LOS. The two equations on the right provide initial conditions for the system's solution. The condition  $I^+(0) = I(0)$  represents the incident radiation from the IR source. The second condition  $I^-(L) = 0$  represents a transparent boundary on the detector's side of the slab. These equations are similar to the classical Kubelka-Munk equations (Klein 1964) for diffuse radiation.

Both  $\alpha$  and  $\beta$  are functions of the radiation wavelength  $\lambda$ . To solve the equations at all desired wavelengths of interest, the Mie theory must be used to evaluate both the cross sections and phase functions at each wavelength. A FORTRAN subroutine has been developed at NRL to compute the

integrals  $\alpha$  and  $\beta$  at each wavelength from the Mie code output. The solution of this coupled linear system of equations gives an expression for the spectral absorbance of the slab geometry

$$A = -\log_{10} \frac{I^+(L)}{I(0)} = -\log_{10} \frac{\Gamma}{\Gamma \cosh(\Gamma L) + b_1 \sinh(\Gamma L)},$$

where  $b_1 = N_p(\sigma_{ab} + \sigma_{sc}(1 - \alpha))$  and  $\Gamma = \sqrt{b_1^2 + N_p^2 \sigma_{sc}^2 \beta^2}$ . If  $\alpha$  and  $\beta$  are zero, then  $\Gamma = b_1$  and this expression for the spectral absorbance reduces to the Lambert-Beer law. Note that the quantities  $\Gamma$  and  $b_1$  are dependent on wavelength  $\lambda$  through the integrals  $\alpha$  and  $\beta$ .

### Brass Extinction Cross Section

The Mie theory calculation of the extinction cross section requires the particle geometry and component material's optical constants as input data. Optical constants for brass were taken from Querry's experimental work (Querry 1985). Figure 10 shows the complex index of refraction for brass as a function of wavelength. The brass used in this experiment came from an M76 IR screening grenade. The brass powder for these grenades is provided by Wolstenholme Bronze Powders (WBP) in two grades. The differences between the two grades are the percentage of stearic acid added as a milling aid and the particle size distribution. The WBP high grease MD7000 brass powder has a mean diameter of 4.17  $\mu\text{m}$ , with 90% of the powder less than 7.25  $\mu\text{m}$ . The Rich MD7000 powder has a mean diameter of 4.83  $\mu\text{m}$ , with 90% of the powder less than 10.26  $\mu\text{m}$  (Edwards et al. 1992).

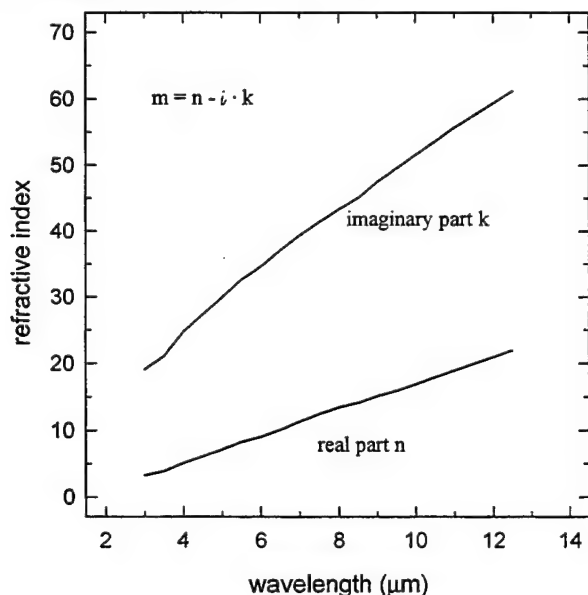


Fig. 10 – The real and imaginary parts of the index of refraction for brass in the 3 - 13  $\mu\text{m}$  region

The extinction cross section, the scattering cross section, and the absorption cross section are calculated as a function of wavelength  $\lambda$  (3.0-14.0  $\mu\text{m}$ ) using an NRL-modified Mie code (Dave 1968). The Mie calculations provide the single-particle albedo  $\omega$ , phase-functions, and asymmetry parameters  $g$  as functions of  $\lambda$ .

Tables 2 and 3 present some results of the Mie computations for nonpolarized radiation in the 3-5  $\mu\text{m}$  and 8-12  $\mu\text{m}$  bands. All of these results are numerical averages of the Mie calculations for the specified particle diameter  $d$  over the respective spectral window. The number of monodispersed particles per cubic centimeter  $N_p$  is based on the experimental mass loading of 135  $\text{g}/\text{m}^3$ .

Table 2 – Results of Mie Calculations for Brass in the 3-5  $\mu\text{m}$  Band

$d$ ( $\mu\text{m}$ )	$N_p$ ( $\text{cm}^{-3}$ )	$\sigma_{\text{ext}}$ ( $\text{m}^2/\text{g}$ )	$\sigma_{\text{sc}}$ ( $\text{cm}^2$ )	$\sigma_{\text{ab}}$ ( $\text{cm}^2$ )	$\omega$	$g$
0.50	$2.43 \times 10^8$	0.061	$2.47 \times 10^{-10}$	$9.03 \times 10^{-11}$	0.6396	-0.2755
0.90	$4.16 \times 10^7$	0.471	$6.97 \times 10^{-9}$	$4.44 \times 10^{-10}$	0.9198	-0.2253
0.954	$3.54 \times 10^7$	0.245	$8.95 \times 10^{-9}$	$5.14 \times 10^{-10}$	0.9307	-0.2140
1.07	$2.50 \times 10^7$	0.269	$1.39 \times 10^{-8}$	$6.69 \times 10^{-10}$	0.9461	-0.1873
1.50	$8.99 \times 10^6$	0.267	$3.88 \times 10^{-8}$	$1.33 \times 10^{-9}$	0.9667	-0.0393
2.30	$2.49 \times 10^6$	0.177	$9.31 \times 10^{-8}$	$2.71 \times 10^{-9}$	0.9717	0.2211
2.90	$1.24 \times 10^6$	0.140	$1.48 \times 10^{-7}$	$1.48 \times 10^{-7}$	0.9729	0.3345
3.70	$5.99 \times 10^5$	0.109	$2.39 \times 10^{-7}$	$6.39 \times 10^{-9}$	0.9742	0.3952
4.83	$2.69 \times 10^5$	0.082	$4.02 \times 10^{-7}$	$1.02 \times 10^{-8}$	0.9750	0.4436

Since the albedo  $\omega$  in Table 2 is close to one for most of the particle sizes considered, the observed spectral extinction in the 3-5  $\mu\text{m}$  band is primarily due to scattering. Particles whose diameters are below 1.5  $\mu\text{m}$  tend to backscatter the IR radiation ( $g < 0$ ). Particles with diameters on the order of 1.5  $\mu\text{m}$  tend to be isotropic scatters ( $g \approx 0$ ), while particles with diameters above 1.5  $\mu\text{m}$  tend to scatter the IR radiation in the forward direction. These results are consistent with the phase functions plotted in Fig. 8.

Table 3 – Results of Mie Calculations for Brass in the 8-12  $\mu\text{m}$  Band

$d$ ( $\mu\text{m}$ )	$\sigma_{\text{ext}}$ ( $\text{m}^2/\text{g}$ )	$\sigma_{\text{sc}}$ ( $\text{cm}^2$ )	$\sigma_{\text{ab}}$ ( $\text{cm}^2$ )	$\omega$	$g$
0.50	0.011	$4.80 \times 10^{-12}$	$5.46 \times 10^{-11}$	0.0750	-0.3036
0.90	0.012	$1.75 \times 10^{-10}$	$2.06 \times 10^{-10}$	0.4112	-0.3283
0.954	0.013	$2.50 \times 10^{-10}$	$2.35 \times 10^{-10}$	0.3719	-0.3282
1.07	0.015	$4.95 \times 10^{-10}$	$3.94 \times 10^{-10}$	0.5617	-0.3268
1.5	0.031	$3.96 \times 10^{-9}$	$6.87 \times 10^{-10}$	0.8108	-0.3096
2.30	0.084	$4.33 \times 10^{-8}$	$2.14 \times 10^{-9}$	0.9441	-0.2500
2.90	0.108	$1.14 \times 10^{-7}$	$3.70 \times 10^{-9}$	0.9665	-0.1888
3.70	0.106	$2.33 \times 10^{-7}$	$5.85 \times 10^{-9}$	0.9754	-0.0780
4.83	0.083	$4.08 \times 10^{-7}$	$9.09 \times 10^{-9}$	0.9782	0.1050

The average mass extinction coefficients  $\sigma_{\text{ext}}$  are comparable for the 0.50  $\mu\text{m}$  and 4.83  $\mu\text{m}$  diameter particles. However, the extinction process for the smaller particle involves significant absorption ( $\omega = 0.64$ ). These calculations demonstrate the difficulty of obtaining unique particle sizes from extinction measurements. The extinction coefficient  $\gamma$  for the 0.5  $\mu\text{m}$  particle is  $0.082 \text{ cm}^{-1}$ . The extinction coefficient for the 4.83  $\mu\text{m}$  diameter particle is  $0.108 \text{ cm}^{-1}$ . In the small particle limit, it is possible to obtain a particle diameter that would give an extinction coefficient identical to that of the larger particle. The calculated

mass extinction coefficients plotted in Fig. 11 as a function of particle diameter readily demonstrate this ambiguity. Any horizontal line intersecting the y axis defines a unique extinction coefficient, but the line intersects the calculated extinction curve at two points, corresponding to a small particle diameter and a large particle diameter. The solution is not unique. In the large and small particle limits, the extinction coefficients, albedo, and phase function become independent of the particle size distribution.

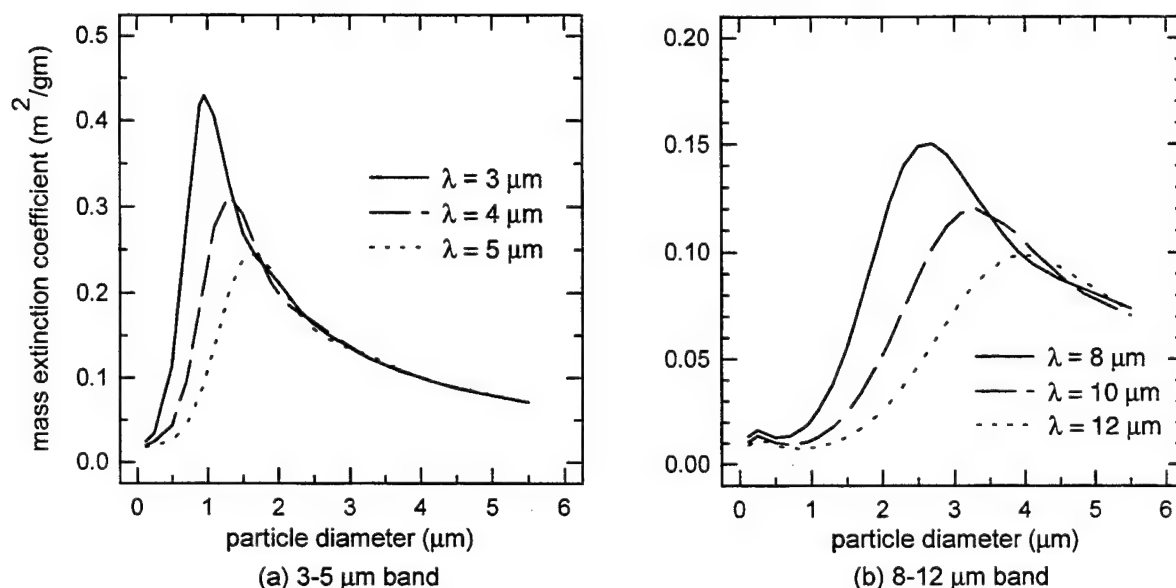


Fig. 11 – Calculated mass extinction coefficients of brass particles as a function of particle size.

Table 3 shows that scattering is dominant for particles larger than 1.5  $\mu\text{m}$  in the 8-12  $\mu\text{m}$  band and absorption is significant for particles below 0.50  $\mu\text{m}$ . The mass extinction coefficient in this band is generally smaller than that of the 3-5  $\mu\text{m}$  band. The extinction coefficient of the 4.83  $\mu\text{m}$  diameter particle is almost identical in both bands, but the asymmetry parameters are quite different. In the 3-5  $\mu\text{m}$  band, the 4.83  $\mu\text{m}$  particle tends to scatter radiation in the forward direction, but the scattering is roughly isotropic in the 8-12  $\mu\text{m}$  band.

### Brass Absorbance Calculations

The spectral absorbance can be calculated from the computed extinction cross section, the particle loading and the geometric path length of the chamber ( $L = 11.4$  cm) using either the Lambert-Beer law model or the two-flux model described above. These calculations depend on the assumed particle size distribution. Since the relative size distribution is unknown, it is assumed to be monodisperse for each calculation. Figure 12 shows the calculated absorbance based on the Lambert-Beer law model for various spherical diameters of brass particles. The experimental mass loading is used to calculate  $N_p$  as a function of particle diameter (Table 2). The calculated absorbances decrease with increasing wavelength for particle diameters below 3.7  $\mu\text{m}$ . This result is consistent with the calculated extinction coefficients given in Fig. 11. At a particle diameter of 4.83  $\mu\text{m}$ , the extinction cross section in the 3-5  $\mu\text{m}$  band is independent of wavelength. In the 8-12  $\mu\text{m}$  band, the extinction cross sections are slightly lower and

roughly equal to each other. The experimental absorbance  $A$  is quite flat over the measured spectral range ( $A = 0.46$ ). The cross section calculated for the  $4.83 \mu\text{m}$  diameter particle gives a flat absorbance. The small diameter particle solution does not give a flat absorbance profile.

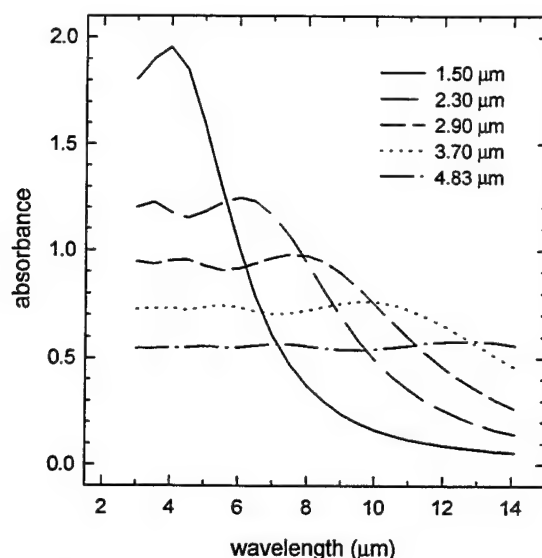


Fig. 12 – Calculated absorbance for a loading of  $135 \text{ g/m}^3$  and pathlength of  $11.4 \text{ cm}$  for various spherical diameters of brass particles based upon the Lambert-Beer law model

The Mie calculations indicate that the extinction by brass particles is dominated by scattering throughout the spectral range ( $3\text{--}12 \mu\text{m}$ ). The absorbance was also calculated from the two-flux model using the same Mie cross sections. The Mie code provided the spectral phase functions for various sphere diameters at each wavelength. These phase functions were averaged over the scattering angle to give the spectral parameters  $\alpha$  and  $\beta$  defined above. Figure 13 shows the two-flux absorbance calculations for the same particle diameters as Fig. 12. The inclusion of the in-scattering term in the radiative transport model lowers the absorbance by 30-50%. Over the  $3\text{--}5 \mu\text{m}$  band, the  $4.83 \mu\text{m}$  diameter particle has a strong forward scattering component (Fig. 8), and the  $\alpha$  parameter is 0.75 and the  $\beta$  parameter is 0.23. The decrease in calculated absorbance over this band from 0.54 for the Lambert-Beer law model to 0.15 for the two-flux model is due to the in-scattering of radiation toward the detector. In the  $8\text{--}12 \mu\text{m}$  band,  $\alpha \approx \beta \approx 0.5$  and the in-scattering terms cancel. The absorbance approaches the Lambert-Beer model.

In Fig. 14, the extinction coefficients derived from the experimental data are compared to those calculated above. Mass extinction coefficients are defined as  $\sigma_{\text{ext}}(\lambda) = 2.303 \cdot A_{\lambda} / L \cdot C$ , where  $A_{\lambda}$  is the measured absorbance at wavelength  $\lambda$ ,  $L$  is the path length, and  $C$  is the mass loading in  $\text{g/m}^3$ . The volume extinction coefficients are calculated by multiplying by the material packing density, either from the literature or measured in this work. The calculated cross section from the  $4.83 \mu\text{m}$  diameter Mie solution was used for both the Lambert-Beer model and the two-flux model. The particle distribution is assumed to be monodispersed. The particle diameter of  $4.83 \mu\text{m}$  gives an almost flat Lambert-Beer law absorbance over the  $3\text{--}14 \mu\text{m}$  wavelength region, which lies above the experimental curve. The effects of the in-scattering term on the absorbance is shown in the same figure by the two-flux model. The absorbance is reduced by a factor of 3.7 in the  $3\text{--}5 \mu\text{m}$  band. This result is readily understood from the asymmetry

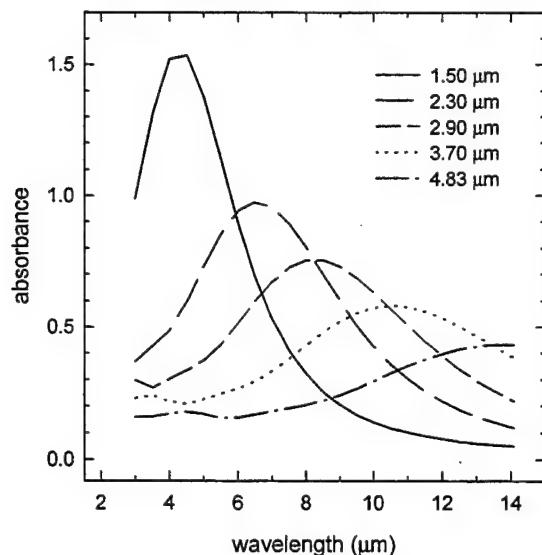


Fig. 13 – Calculated absorbance for the same particle diameters as Fig. 12 using the two-flux model

parameter  $g = 0.444$  of Table 2 and the phase function depicted in Fig. 8. In the 3-5  $\mu\text{m}$  band, the 4.83  $\mu\text{m}$  diameter brass powder scatters radiation into the forward direction. In the 8-12  $\mu\text{m}$  band, the asymmetry parameter is 0.105 and the forward scattering component of the intensity is less. Thus, the reduction in absorbance is not as great. The experimental absorbance lies between these two theoretical absorbance models. Only single scattering processes are considered in the two-flux model. The inclusion of multiple scattering would increase the absorbance in the 3-5  $\mu\text{m}$  band. The effects of particle size distribution on the calculation have not been fully explored.

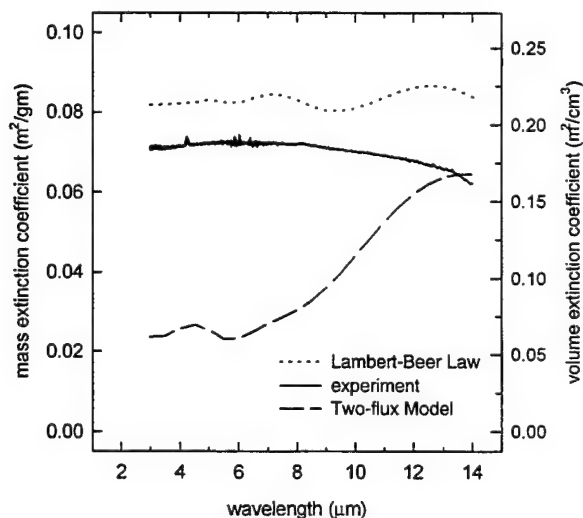


Fig. 14 – Comparison of the extinction coefficients calculated from the measured absorbance of brass flakes with the results of the two models assuming 4.83  $\mu\text{m}$  diameter particles

The mass extinction coefficient calculated for brass particles with a mean diameter of 4.83  $\mu\text{m}$  in both the 3-5  $\mu\text{m}$  band and the 8-12  $\mu\text{m}$  band is 0.082  $\text{m}^2/\text{g}$ . The values reported by Edwards et al. are 1.13  $\text{m}^2/\text{g}$  (3-5  $\mu\text{m}$ ) and 1.34  $\text{m}^2/\text{g}$  (8-12  $\mu\text{m}$ ). These latter values are higher than ours by a factor of 14-16. However, our experimental results are consistent with the theoretical Mie calculations and the mean particle size provided by WBP. The agreement of the calculated brass absorbance and the experimental absorbance provides strong evidence that our mass extinction coefficient is correct.

### Boron Nitride Calculations

Boron nitride has four crystal structures (Doll 1994): hexagonal, cubic, wurtzitic, and rhombohedral. In the hexagonal form, it is a slippery white solid with a layered structure very similar to graphite (Cotton and Wilkinson 1972). At high temperature and pressure, the hexagonal form is converted to a cubic form with a diamond structure. The cubic form is very hard and will scratch diamond. BN is stable in dry air, but is slowly hydrolyzed by water to produce boron oxides. The hexagonal form is commercially available from The Carborundum Company, Amherst, NY. Several references on the dielectric properties of the hexagonal form are available in the open literature (Geick, et al. 1966; Hoffman et al. 1984). The optical constants of cubic BN over a photon energy range of 2.5-20 eV has been reported by Miyata et al. (1989). Geick et al. (1966) have performed a Kramers-Kronig analysis of the IR reflection spectra of hexagonal BN from 100-3000  $\text{cm}^{-1}$ . The analysis provides the complex dielectric functions  $\epsilon(\lambda)$  for IR radiation polarized parallel and perpendicular to the hexagonal  $c$  axis. These dielectric functions are represented by a classical oscillator fit with resonances at 12.8  $\mu\text{m}$  ( $E$  parallel to  $c$ ) and 7.2  $\mu\text{m}$  ( $E$  perpendicular to  $c$ ) over a spectral range 5 -33  $\mu\text{m}$ . The absorption spectrum exhibits several minor peaks that are probably due to 2-phonon combination processes. Hoffman et al. (1984) have performed optical reflectance studies of the  $c$  face of BN over a photon energy range of 0.045-10 eV and obtained dielectric functions that are quite similar to those of Geick et al. However, we question the accuracy of their data over the 3-5  $\mu\text{m}$  range. They report a large absorption feature that we do not observe in IR transmission and cannot explain on theoretical grounds. Their sample may have been contaminated.

The complex index of refraction  $m = n - i \cdot k$  can be calculated from the square root of  $\epsilon(\lambda)$ . The optical constants of hexagonal BN have been calculated over the 5-12  $\mu\text{m}$  range using the dielectric functions provided by the Geick et al. oscillator models. Because these data are not published, it is tabulated in Table 4 for reference.

The Mie theory is applicable to a homogeneous spherical particle. If the particles are small compared to the wavelength, the exact Mie theory of scattering reduces to an electrostatic approximation (Rayleigh limit). If the particle is a small, homogeneous, isotropic sphere, the incident radiation presents a uniform electric field to the particle and induces an electric polarization that results in a dipole parallel to the incident field. Since the sphere's dielectric function is a scalar quantity, its polarizability does not depend on its orientation. In the Rayleigh limit, the cross sections for extinction and scattering are directly related to the polarizability. Thus, for a spherical particle composed of *isotropic* material, the cross sections are independent of the sphere's orientation. Hexagonal BN is an *anisotropic* material. The polarizability of hexagonal BN depends on the orientation of the incident field relative to the  $c$ -axis (Table 4). The dipole induced within a spherical particle of BN by the incident field is not, in general, parallel to that field. The polarizability is a tensor. Determination of the extinction and scattering cross sections under these conditions requires some care. The polarizability of an anisotropic sphere can be calculated exactly in the electrostatic approximation. The average extinction cross section of a collection of randomly orientated, sufficiently small, anisotropic spheres is (Bohren and Huffman 1983)



$$\langle C_{ext} \rangle = \frac{C_{parallel}}{3} + \frac{2 \cdot C_{perpendicular}}{3},$$

where  $C_i$  denotes the cross section of an isotropic sphere with  $i$ -th polarization. This formula is valid for particles that are small compared to  $\lambda$ . In hexagonal BN, the two principal directions perpendicular to the  $c$  axis are equivalent (2/3). Fig. 15 compares the average mass extinction coefficient,  $\langle C_{ext} \rangle$ , with the experimentally determined value. The mass extinction coefficients were calculated at specific wavelengths using the derived optical constants (Table 4) and a particle size distribution function provided by The Carborundum Company.

Table 4 – Calculated BN Complex Index of Refraction

Wavelength ( $\mu\text{m}$ )	Electric field perpendicular to $c$ axis		Electric field parallel to $c$ axis	
	$n$	$k$	$n$	$k$
6.0	1.037	0.099	1.426	0.183
6.5	0.215	1.454	1.671	1.690
7.0	0.603	3.829	2.740	0.309
7.5	6.212	1.113	2.410	0.088
8.0	4.012	0.167	2.276	0.044
8.5	3.459	0.074	2.197	0.029
9.0	3.202	0.045	2.136	0.021
9.5	3.049	0.033	2.080	0.018
10.0	2.944	0.027	2.017	0.017
11.0	2.791	0.027	1.813	0.024
12.0	2.617	0.068	0.902	0.196
12.5	2.449	0.214	0.520	2.646
13.0	2.788	0.815	4.361	0.468

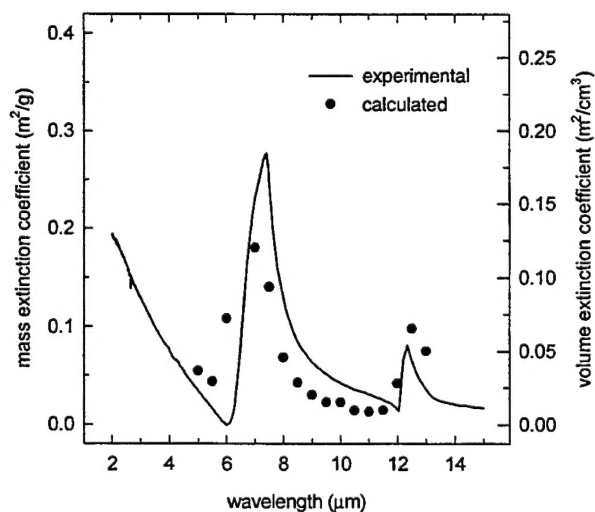


Fig. 15 – Comparison of experimentally determined mass extinction coefficients for BN powder and those calculated in this work

## DISCUSSION

The experimental results and theoretical model presented above indicate that we are capable of experimentally determining and theoretically understanding the potential of various powders as infrared obscurants. Several general, but important observations must be considered about the work conducted so far. The data presented in Fig. 4 verify that laboratory measurements on a small scale can be used to predict the effectiveness of the obscurants when deployed in a large-scale test. The ability to find powders with structured resonances throughout the IR provides the confidence that we can choose chemical characteristics to tailor the spectral response of the material in a wide variety of ways. Finally, the success of the theoretical model in predicting structures and cross sections will provide a valuable tool in screening future candidates and their appropriate size distributions. In this section, we briefly discuss the impact of the results, some recommendations for candidates, and directions for future work in this area.

The most surprising result from this work is the determination of the cross section for scattering by brass. Brass was chosen as a baseline system, one that we believed was not extremely useful from a Navy point of view, but one that we need to understand because it is widely used and documented. The cross sections we measure are about a factor of 16 lower than those reported (Edwards 1992). However, the ability of the theoretical model to predict the experimental observations within 10% provides convincing evidence that the reported values are incorrect. The reasons for this error are not yet understood, but may relate to the fact that the original data were taken in a very dense, very long path length cloud, which absorbed >98% of the incident radiation. Under these conditions, several possible scenarios emerge. First, the amount of radiation on the IR detector might be close to the noise floor of the system. This cannot be proven without access to the original data. Second, multiple scattering effects may have played some part in the experiment. This does not seem to be likely since the model developed in our work indicates that this is not a problem in our experiment where the mass loadings are higher (but with much shorter path lengths). Third, the sample we obtained may not be identical to that for which data are reported in the literature. Because the obscuration in brass is based solely on scattering, the particle size and geometry might be expected to play a large role in determining the cross section. We have theoretically looked into some of these problems, and differences are evident for spherical particles vs ellipsoidal particles or flat flakes. However, these differences are not large enough to account for the discrepancy. Regardless of the reasons for the differences, it is clear that the brass flakes are not as effective an obscurant as is popularly believed. The primary reason brass was chosen over graphite by the Army was its packing density, which is about three times that of graphite. Since the cross section for graphite is reported to be between 1.4 and 2.6 m<sup>2</sup>/gm, and we measure 0.08 m<sup>2</sup>/gm for brass, graphite is clearly much more attractive. We plan to acquire various graphite powders and flakes and perform an identical analysis on them to confirm the reported cross section measurements. Should these experiments agree with the reported values, we would recommend the graphite as an alternative to brass flakes. However, as with the brass, the graphite powders seem to rely solely on scattering for obscuration, with no obvious resonances in the 3-5  $\mu$ m spectral region.

We performed similar experimental and theoretical studies on boron nitride powder, which was one of our initial candidates. We found that the spectra in the literature (Doll 1994) were incorrect; however, we were able to derive good optical constants to model its absorption and scattering characteristics. Figure 15 shows the agreement between theory and experiment. While boron nitride itself does not have strong resonances in the 3-5  $\mu$ m region, it does exhibit a strong resonance at 7.4  $\mu$ m ( $\sigma_{\text{ext}} = 0.27 \text{ m}^2/\text{gm}$ ) which tails into the 10  $\mu$ m region. This may, therefore, be useful in the long wave IR. The available optical constants cover only wavelengths longer than 5  $\mu$ m, but the Mie calculation includes the particle size distribution for this sample provided by the manufacturer. Considering the complexity of the problem, the agreement is excellent. This also confirms that our model is capable of providing useful guidelines for

predicting accurate cross sections for both scattering and absorption features through the entire IR region, provided the complex index of refraction and particle size distribution are available. We are confident that we can now use the theory to prefilter candidate materials and provide specific guidelines concerning the optimum particle sizes for these materials.

The data shown in Fig. 5 for boric acid reveal several absorption peaks in the regions of interest. It should be noted that this sample was not analyzed to determine its size distribution, and so could not accurately be modeled. Although the spectra appear promising, the cross sections are too low (typically  $\sim 0.008 \text{ m}^2/\text{gm}$ ) to make it an effective obscurant. However, it could be used for demonstration purposes or proof-of-principle tests. We are optimistic that this is not the best system available in this region, and are looking at several alternatives. This molecule is also a good test case to determine our ability to enhance the cross sections by increasing the scattering part of the extinction. This system may also be useful as a model for the types of bonds that will exhibit strong absorption in the 3-5  $\mu\text{m}$  and 8-12  $\mu\text{m}$  regions.

Currently we are screening additional materials for possible application to this problem. Materials that appear promising are inorganic amine powders, plastic spheres, graphitic species, and some minerals. Liquid aerosols may also be promising sources as possible obscurants. In many cases, spectra are not available for these species, and we will need to determine these, as well. It does appear that the methodology and approach we have described is both sound and practical and can be applied to a number of problems. We also propose to extend this technique to other regions of the spectrum, including the near IR, visible, and UV. These extensions appear to be straightforward applications of the current experimental setup, with some additional optics to cover the expanded portions of the spectrum.

## REFERENCES

- C. F. Bohren and D. R. Huffman, *Absorption and Scattering of Light by Small Particles* (John Wiley and Sons, New York, NY, 1983) p. 184.
- M. Q. Brewster, *Thermal Radiative Transfer & Properties* (John Wiley and Sons, New York, NY, 1992).
- Chemical Engineers' Handbook* 5th ed., R. H. Perry and C. H. Chilton, eds. (McGraw-Hill, New York, NY, 1973) pp. 5-62.
- F. A. Cotton and G. Wilkinson, *Advanced Inorganic Chemistry*, 3rd ed. (John Wiley and Sons, New York, NY, 1972) p. 229.
- J. V. Dave, "Subroutines for Computing the Parameters of the Electromagnetic Radiation Scattered by a Sphere," Report No. 320-3237, IBM Palo Alto Scientific Center, Palo Alto, CA, 1968.
- G. L. Doll, "Optical functions of BN," in *Properties of Group III Nitrides*, J.H. Edgar, ed. (Institution of Electrical Engineers, London, 1994) pp. 169-174.
- H. Edwards, A. B. Marshall, A. K. Rowlands, and J. D. Collins, "Fast Bloom VIS/IR Obscurant Screens," in *Proceedings of the Smoke/Obscurants Symposium XVI*, Vol. 2, pp. 515-556 (AD B176968).
- R. Geick, C. H. Perry, G. and Rupprecht, "Normal Modes in Hexagonal Boron Nitride," *Phys. Rev.* **146**, 543-547 (1966).

J. D. Klein , "Radiation Heat Transfer Through Scattering and Absorbing Nonisothermal Layers," in *Symposium on Thermal Radiation of Solids*, S. Katzoff, ed., NASA SP-55 (AD 629980).

N. Miyata, K. Moriki, O. Mishima, M. Fujisawa, and T. Hattori., "Optical Constants of Cubic Boron Nitride," *Phys. Rev. B* **40**, 12028-12209 (1989).

M. N. Ozisik, *Radiative Transfer and Interactions with Conduction and Convection* (John Wiley and Sons, New York, NY, 1972) p. 261.

PDEase (1995), available from Macsyma Inc., 20 Academy Street, Arlington, MA 02174.

M. R. Querry, "Optical Constants," Technical Report CRDC-CR-85034, U.S. Army Chemical Research, Development and Engineering Center, Aberdeen Proving Ground, MD (1985)

L. X. Zhou, *Theory and Numerical Modeling of Turbulent Gas-Particle Flows and Combustion* (CRC Press, Inc., Boca Raton, FL, 1993) p. 111.

M. J. Zucrow and J. D. Hoffman, *Volume 1 Gas Dynamics* (John Wiley and Sons, New York, NY, 1976) pp. 545-548.